Journal of Quantitative Spectroscopy & Radiative Transfer 120 (2013) 70–80

Contents lists available at SciVerse ScienceDirect

Journal of Quantitative Spectroscopy & Radiative Transfer

journal homepage: www.elsevier.com/locate/jqsrt

Engineering the broadband spectrum of close-packed plasmonic honeycomb array surfaces

Rüştü Umut Tok, Kürşat Şendur*

Faculty of Engineering and Natural Sciences, Sabancı University, Orhanlı, Tuzla, 34956 Istanbul, Turkey

ARTICLE INFO

Article history:
Received 12 September 2012
Received in revised form
17 January 2013
Accepted 20 January 2013
Available online 13 February 2013

Keywords:
Broadband
Spectroscopy
Plasmonics
Nanoantennas

ABSTRACT

Plasmonic nanostructures operating over a wide spectrum are promising candidates for broadband spectroscopic applications. While promising, spectral engineering of close-packed plasmonic honeycomb nanoantenna arrays is challenging due to the strong correlation between the particle geometry and hexagonal grid, particle coupling within unit cells, and interaction between neighboring unit cells. In this study, we demonstrate that the spectral distribution of large scale surfaces can be effectively tailored over a wideband spectral range using close-packed plasmonic honeycomb array surfaces. We discuss coupling-mechanisms responsible for the spectral response of honeycomb arrays and discuss the geometrical restrictions limiting the bandwidth of the spectral response. These limitations can be overcome with a more general honeycomb structure by introducing additional morphological parameters within the Wigner–Seitz unit cell. The proposed morphological parameters provide additional flexibility for manipulating the spectrum by relaxing geometrical restrictions due to a strong correlation between the unit-cell and nanoparticle morphology. Furthermore, we achieve spectral broadening by breaking the symmetry within a Wigner–Seitz unit cell on a hexagonal grid, rather than breaking the symmetry of the hexagonal grid itself via generalized honeycomb arrays. Additionally, we demonstrate the advantages of close-packed arrays in terms of spectral response and electric field enhancement over large surfaces. Finally, radiative far-field properties, absorptance, transmittance, and reflectance of honeycomb structures are investigated.

1. Introduction

Nanoparticles and artificial structures composed of a special arrangement of nanoparticles are one of the most fascinating fields for scientists and engineers due to their unique optical properties [1–3]. Among these nanosystems, plasmonic nanoparticles of different shapes have recently attracted significant interest due to the tunability of their resonances, their ability to manipulate light beyond the diffraction limit, and strong electromagnetic fields associated with their optical resonances [4–6]. The two dimensional surface arrangement of plasmonic structures [7] demonstrates many interesting optical properties such as extraordinary transmission through subwavelength hole arrays at optical wavelengths [8], localization of electromagnetic energy to subwavelength regions [9], electrically induced transparency at the optical regime [10,11] and negative refractive index metamaterials [12]. These exciting properties of plasmonic nanoparticles and the arrangement of nanoparticles for desired optical properties have opened up the fields of plasmonics [13–15] and optical metamaterials [12] in the quest for materials with improved optical functionality.

Optical nanoantennas [16–18] and radiative energy transfer at the nanoscale [19–23] have led to significant advances in nanotechnology. Recent advances in plasmonic

* Corresponding author. Tel.: +902164839527.
E-mail address: sendur@sabanciuniv.edu (K. Şendur).

0022-4073/$ - see front matter © 2013 Elsevier Ltd. All rights reserved.
http://dx.doi.org/10.1016/j.jqsrt.2013.01.026

and photovoltaic devices involving a wideband absorption spectrum, such as solar cells [24] and nonlinear process enhancement [25], have increased the research on broadband plasmonic structures [26–33].

To address the aforementioned need for a unidirectional wideband absorption and field enhancement spectrum over a large surface area, we proposed [29] a plasmonic honeycomb antenna array with broken symmetry. The honeycomb nanoantenna array, shown in Fig. 1, is based on a hexagonal grid with periodically arranged plasmonic antennas as Wigner–Seitz cell building blocks. This design offers advantages in terms of wideband spectral operation, unidirectional field patterns, and field enhancement over a large surface area. Due to the broken symmetry of the Wigner–Seitz cell, multiple resonances are supported by the plasmonic honeycomb antenna array over a broad spectrum [29]. The constructive interference of the vectoral superposition of the fields produced by the Wigner–Seitz unit cells provides the unidirectional feature of the wideband spectrum over the plasmonic antenna surface.

In our previous study [29], simple rod-like structures were utilized. As is well-known in the literature, particle shape plays an important role in spectrum engineering. Changing particle geometry in close-packed antenna arrays, however, has challenges. This challenge is due to the strong correlation of the particle shape and length with the repeating unit cell geometry. In other words, the morphology of the nanoantenna particles and array unit cells are strongly dependent on each other. As we will discuss in this article, the length of the particle cannot be arbitrarily changed and is limited by the geometric constraints on the unit cell geometry. This constraint limits the spectral tunability of close-packed arrays. In this study, we propose a generalized close-packed honeycomb array by introducing additional morphological parameters within the Wigner–Seitz unit cell. The generalized honeycomb plasmonic antenna array provides additional flexibility in the manipulation of the spectral response via these new morphological parameters by relaxing geometrical restrictions due to particle length and angles within the Wigner–Seitz unit cell.

Another contribution of this study is the suggestion of an alternative technique for breaking the symmetry of plasmonic honeycomb antenna arrays. In this study, we have demonstrated that spectral broadening can also achieved by breaking the symmetry within the Wigner–Seitz unit cell on a hexagonal grid, rather than breaking the symmetry of the hexagonal grid itself. Also in this study, the advantages of close-packing the antenna arrays are demonstrated in terms of spectral response, field enhancement, and absorption over a large surface area. In addition, we discuss the coupling mechanism of the plasmonic antenna array elements in forming the spectral features. Also in this study, radiative far-field properties such as absorptance, transmittance, and reflectance of honeycomb structures are investigated.

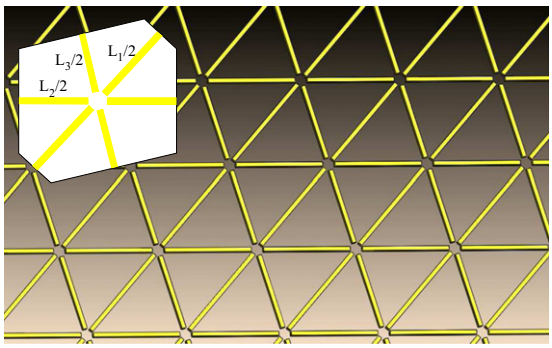

Fig. 1. A honeycomb array consisting of rod like particles and the corresponding unit cell (inset).

The paper is organized as follows. In Section 2, a summary of the solution technique is provided. In Section 3, the coupling mechanisms are discussed for the plasmonic honeycomb antenna arrays in forming the spectral features over a broad spectrum. Also in this section, we introduce geometrical restrictions on asymmetrical Wigner–Seitz unit cells. Then we clarify the spectral features of the honeycomb array in terms of couplings between the individual particles and discuss the limitations of geometrical restrictions on spectral response. In Section 4, we propose a more general family of honeycomb arrays by introducing additional parameters within the unit cell. In this section, spectral broadening is achieved by breaking the symmetry of the morphology within Wigner–Seitz unit cells where the hexagonal grid can be kept symmetric. By employing this type of symmetry breaking, geometrical restrictions which reduce the flexibility of spectral tailoring are relaxed. In Section 5, we demonstrate the advantages of close-packed arrays in terms of spectral response and field enhancement over large surfaces. In Section 6, we investigated the far-field radiative properties of honeycomb plasmonic nanoantenna array, such as absorptance, transmittance, and reflectance.

2. Methodology

In this study a 3-D frequency domain finite element method based on a full-wave solution of Maxwell's equations is used to obtain near field enhancement and far-field absorptance, transmittance, and reflectance of the honeycomb structures. The accuracy of the solution technique was previously validated by comparison with other solution techniques [34,35]. To calculate the scattered field $\vec{E}_s(\vec{r})$, the honeycomb structure is illuminated with a circularly polarized plane wave at the normal incidence to the plasmonic array surface to effectively excite all of the particles oriented in different directions. Once the scattered field is obtained, the total electric field $\vec{E}_t(\vec{r})$ is calculated as $\vec{E}_t(\vec{r}) = \vec{E}_i(\vec{r}) + \vec{E}_s(\vec{r})$ where $\vec{E}_i(\vec{r})$ is the incident plane wave. For the analysis of the nanoantenna array, periodic boundary conditions are used to reduce the computational time and memory demands. This boundary condition mimics the periodic nature of the nanoantenna array, by analyzing a single Wigner–Seitz unit cell, rather than by analyzing a layer containing large numbers of repeating antenna geometries. To account for the presence of neighboring unit cells, three periodic boundary conditions are defined on the three mutual, face-to-face lateral surfaces of the hexagonal shaped Wigner–Seitz unit cell. On the top

and bottom surfaces of the unit cell, radiation boundary conditions are used. In the solution procedure tetrahedral elements are used to discretize the computational domain, which accurately represents the scattering geometries used in this study. On the tetrahedral elements, edge basis functions and second-order interpolation functions are used to expand the field distributions. Adaptive mesh refinement is used to improve the coarse solution regions with high field intensities and large field gradients. The material of the honeycomb structure is chosen as gold and the structure is simulated as in a vacuum. The dielectric constant of gold is chosen from the experimental data by Palik [36].

To quantify the results the average field enhancement (AFE) is introduced which is a measure of field enhancement over the entire surface of the honeycomb array. AFE is defined by the following equation:

$$\mathrm{AFE} = \frac{1}{\mathrm{S}} \int_{\mathrm{UC}_a} \frac{|\vec{E}_t(\vec{r})|^2}{|\vec{E}_i(\vec{r})|^2}\, dA \tag{1}$$

where UC_a represents the surface just above the honeycomb array within a Wigner–Seitz unit cell and S is the area of that surface. The absorptance, transmittance, and reflectance of the honeycomb structure are calculated by applying the electromagnetic power relations [37] to the honeycomb unit cell geometry:

$$A = \frac{1}{2P_i}\omega \Im\{\epsilon_{gold}\} \int_{\mathrm{HC}} |\vec{E}_t(\vec{r})|^2\, dV \tag{2}$$

$$T = \frac{1}{P_i} \int_{\mathrm{UC}_b} \frac{1}{2} \Re\{\vec{E}_t(\vec{r}) \times \vec{H}_t^*(\vec{r})\} \cdot d\vec{A} \tag{3}$$

$$R = -\frac{1}{P_i} \int_{\mathrm{UC}_a} \frac{1}{2} \Re\{\vec{E}_s(\vec{r}) \times \vec{H}_s^*(\vec{r})\} \cdot d\vec{A} \tag{4}$$

Here, HC stands for the total volume of the gold particles within a unit cell, UC_b represents the surface just below the honeycomb array within a Wigner–Seitz unit cell, and $\vec{H}_t(\vec{r})$ and $\vec{H}_s(\vec{r})$ are the total and scattered magnetic fields, respectively. $\Re$ and $\Im$ represents the real and imaginary parts of the quantities, respectively. P_i is the incident power given by the following equation:

$$P_i = \int_{\mathrm{UC}_a} \frac{1}{2} \Re\{\vec{E}_i(\vec{r}) \times \vec{H}_i^*(\vec{r})\} \cdot d\vec{A} \tag{5}$$

3. Coupling-mechanisms shaping the spectral response of the honeycomb array

Fig. 2 illustrates the parameters that can be used to tune the spectral response, which include the length of the gold nanoparticles, the angle between the particles, and the gap diameter. As illustrated in Fig. 2, the particle lengths and angles between the particles depend on each other according to the following equation:

$$R = \frac{L_1/2+g/2}{\cos(\alpha_1/2)} = \frac{L_2/2+g/2}{\cos(\alpha_2/2)} = \frac{L_3/2+g/2}{\cos(\alpha_3/2)} \tag{6}$$

There are also constraints on angles α_1, α_2, and α_3 such that $\alpha_1+\alpha_2+\alpha_3 = 180^\circ$ and also any of these angles can not be arbitrarily small otherwise individual particles will overlap. These constraints on angles and lengths of particles restrict the Wigner–Seitz unit cell geometry. When the antennas are placed in the form of a honeycomb array, the length of particles and the angle between them are strongly correlated. If lengths of the antennas are varied, the angles between them change too, which impacts coupling strengths between different antennas. This is not the case when the antennas are isolated. For an isolated asymmetric snowflake nanoantenna, the angles between the antenna arms can be kept equal even though the antenna length can be different. In this manner, one could observe and tailor the resonance peaks corresponding to each particle [28]. For an isolated asymmetric snowflake nanoantenna, these peaks correspond to the fundamental modes of the particles with lengths L_1, L_2, and L_3, since the coupling between antenna arms is weak.

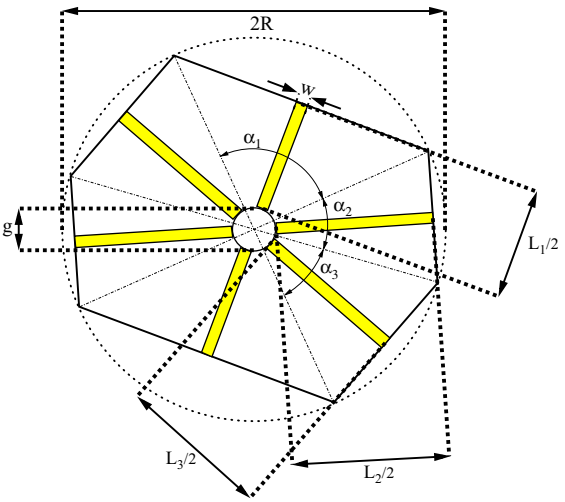

Fig. 2. Geometric parameters within the Wigner–Seitz unit cell of an asymmetric close-packed honeycomb array. R, g, and L are unit cell radius, gap diameter, and lengths of the antennas, respectively. α's are the angles such that the angle between the successive antennas i and j is $(\alpha_i+\alpha_j)/2$.

When the antennas are arranged as a closed-packed honeycomb lattice, the length of particles and the angle between them are strongly correlated. Due to the geometrical correlation between the antenna arm lengths and the angle between them as identified in Eq. (6), the plasmonic antenna lattice prevents the formation of an equiangular structure. This leads to a change in the coupling strengths between the particles, which in turn shift the peaks of the spectral response. In a honeycomb array, if an asymmetry is introduced to the antenna lengths, the angles between them are no longer equal to each other. Such a change in angles leads to differences in the coupling strengths between the particles within the unit cell. When the angle between antenna arms gets smaller, the coupling between the antenna arms becomes stronger. Due to strong interaction between the antenna arms, the resonance peaks corresponding to the modes interact and shift. In this section, the coupling-mechanisms between the antenna elements within a unit cell are discussed.

To illustrate the correlation between the antenna arm length and the spectral coupling due to the angle between antenna elements, in Fig. 3 the AFE of four asymmetric honeycomb arrays with different asymmetries are shown with black, red, blue and green curves. The lengths, $[L_1\ L_2\ L_3]$, of the particles in these structures corresponding to these curves are [180 185 190] nm, [180 190 200] nm, [180 200 220] nm, and [180 210 240] nm, respectively. The thickness, t, and width, w of the particles are 20 nm and 10 nm respectively, and the gap diameter, g, is 30 nm. In Fig. 3, as the asymmetry increases, the angle between L_2 and L_3 gets smaller, the angle between L_1 and L_2 increases, and the angle between L_1 and L_3 remains almost constant at 60°. This leads to a strong coupling between L_2 and L_3, which causes the peaks of L_2 and L_3 to move away from each other. Due to this shift of the L_2 peak, the peaks corresponding to L_1 and L_2 overlap.

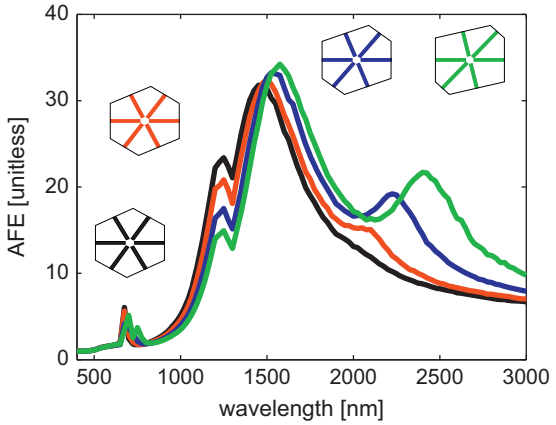

Fig. 3. AFE of close-packed honeycomb structures with various asymmetries. The thickness and width of the gold nanoantennas are 20 nm and 30 nm respectively and the gap diameter is 30 nm. Antenna lengths $[L_1\ L_2\ L_3]$ are [180 185 190] nm, [180 190 200] nm, [180 200 220] nm, and [180 210 240] nm for black, red, blue, and green honeycombs, respectively. (For interpretation of the references to color in this figure caption, the reader is referred to the web version of this article.)

To further understand the coupling between antenna elements, we investigated the contribution from individual sub-arrays by applying a recent sub-domain decomposition technique [38] to large scale arrays. For this purpose, the case shown in Fig. 4(a) in which the AFE spectrum (green curve) of an asymmetrical honeycomb (Fig. 4(b)) is investigated. The lengths of the particles in the honeycomb are [180 210 250] nm, the thickness, t, the width, w, and the gap diameter, g, of the structure are 20 nm, 10 nm, and 30 nm, respectively. In this case the angles between the antennas $[(\alpha_1+\alpha_2)/2\ (\alpha_1+\alpha_3)/2\ (\alpha_2+\alpha_3)/2]$ are [76.6352° 56.5046° 46.8603°], respectively. Since a honeycomb plasmonic nanoantenna array is a close-packed structure, each particle within a Wigner–Seitz cell is also coupled to the particle in the neighboring unit cell, which is analogous to a crystal structure formed by atoms. Therefore, analyzing this problem in terms of the coupling between the sub-arrays provides a good understanding in terms of contributing factors. An additional coupling mechanism, the coupling between the unit cells due to the close proximity of neighboring unit cells, is later investigated in Section 5.

In Fig. 4(a), the AFE of each sub-array is given. The black, red and blue curves in Fig. 4(a) correspond to the AFEs of the sub-arrays S_1 (shown in Fig. 4(c)), S_2 (shown in Fig. 4(d)), and S_3 (shown in Fig. 4(e)), respectively. Each sub-array contains only one type of particles. S_1 contains only particles with length L_1, whereas S_2 and S_3 contain only particles with lengths L_2 and L_3, respectively. The individual peaks of resonance wavelengths corresponding to each sub-array (black, red and blue curves of Fig. 4(a)) are not observable at the corresponding wavelengths in the AFE spectrum of the combined structure (green curve of Fig. 4(a)). The difference is attributed to coupling between the sub-arrays (or coupling between the particles within the unit cell).

To understand how these fundamental modes interact with each other, the coupling of sub-array pairs are investigated next. AFE spectrums of pair-wise combinations of sub-arrays are illustrated in Fig. 5(a). Black, red and blue curves of Fig. 5(a) demonstrate the AFE spectrums of sub-

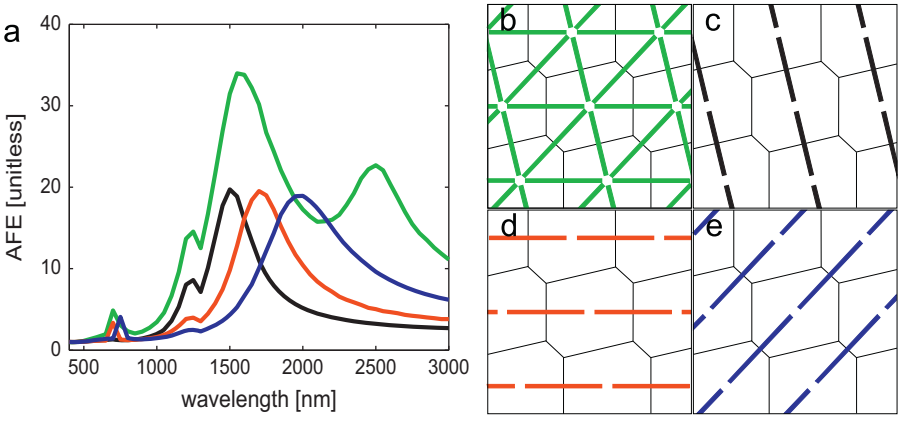

Fig. 4. AFE of a close-packed honeycomb array (green) and its constituents sub-arrays S_1 (black), S_2 (red), and S_3 (blue) (a), schematic representations of close-packed honeycomb array (b), sub-array S_1 (c), sub-array S_2 (d), and sub-array S_3 (e). (For interpretation of the references to color in this figure caption, the reader is referred to the web version of this article.)

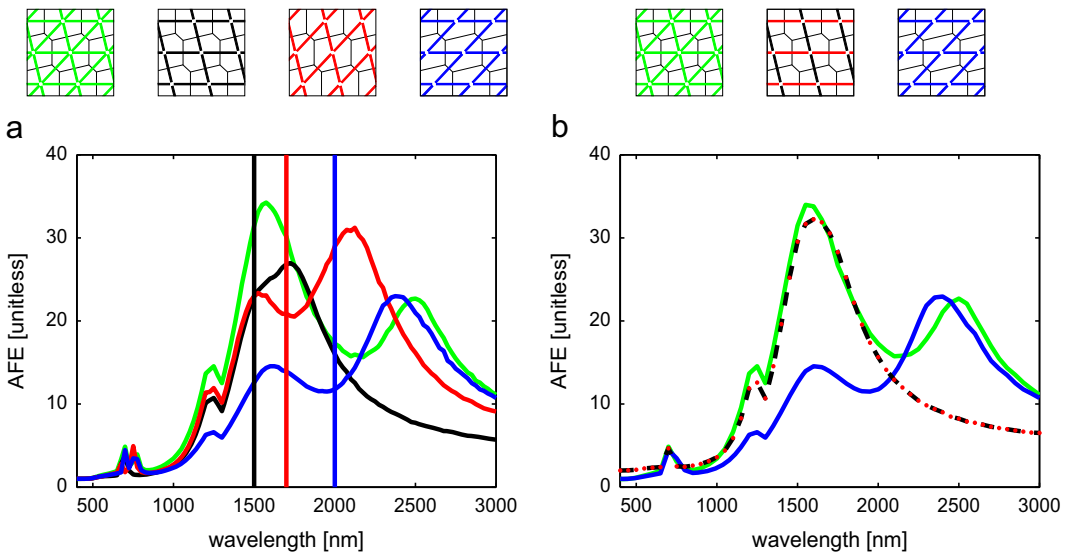

Fig. 5. AFE of close-packed honeycomb array (green) and sub-arrays S_{12} (black), S_{13} (red), and S_{23} (blue), for comparison spectral peak positions of S_1, S_2, and S_3 sub-arrays are shown as black, red, and blue vertical lines respectively (a), Spectral responses of close packed honeycomb array (green) and sub-arrays S_1 plus S_2 (black-red dashed dotted) and S_{23} (blue) which the honeycomb array can be decomposed into (b). (For interpretation of the references to color in this figure caption, the reader is referred to the web version of this article.)

arrays [S_{12}], [S_{13}], and [S_{23}], respectively. The structures of these sub-arrays are shown in Fig. 5(a) with the related colors. Black, red, and blue vertical lines in Fig. 5(a) illustrate the resonance peaks of S_1, S_2, and S_3 when they are isolated. The results in Fig. 5 suggest that the coupling between sub-array S_2 and S_3 is strongest since the angle between the orientations of S_2 and S_3 is smallest. Furthermore, the coupling between S_1 and S_3 is weaker and the coupling between S_1 and S_2 is weakest according to the angles between sub-arrays. From the blue curve we can infer that S_2 and S_3 interact strongly because the peaks of the structure [S_{23}] differ remarkably from the individual peak of S_2 and S_3. Due to the coupling the peaks shift away from each other. From the red curve of Fig. 5(a), we can infer S_1 and S_3 interact but not as strongly as S_2 and S_3 since the peaks of individual sub-array shift slightly. The results corresponding to the black curve suggest that S_1 and S_2 interact weakly because the peaks remain almost at the same position where they were when the corresponding sub-arrays are isolated.

Based on this discussion, the contributions to the spectral features of the honeycomb structure considered in this case are identified. As illustrated in Fig. 5(b) the peak at longer wavelengths is mainly attributed to coupling between S_2 and S_3. Due to this strong coupling, the peak of S_3 shifts to longer wavelengths and forms the second peak. In the mean time, the peak of S_2 shifts toward the peak of S_1; they overlap and form the first peak at shorter wavelengths. In Fig. 5(b) it is also demonstrated that the magnitude of the first peak is close to the summation of the peak values of S_1 and S_2 (black and red dotted dashed curve of Fig. 5(b)) as they were isolated since the interaction between these sub-arrays is small.

The antenna elements are also strongly coupled with the gap dimensions as shown in Fig. 6. In Fig. 6 the AFE

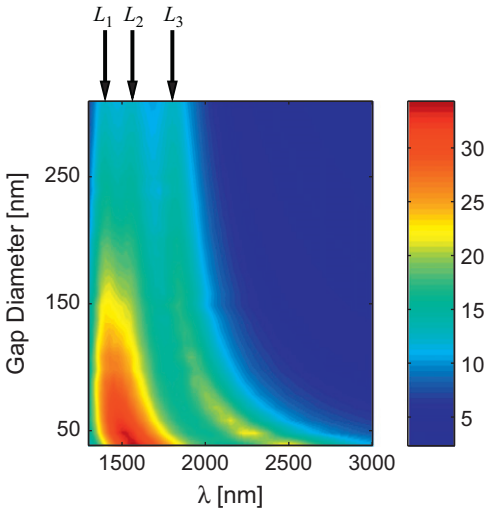

Fig. 6. AFE of a close-packed honeycomb array with respect to gap diameter. The thickness and the width of the gold nanoantennas are 20 nm and 30 nm respectively and antenna lengths are [180 210 250] nm.

spectrum of the same honeycomb array is given with respect to the gap diameter. As we increase the gap diameter, coupling between the particles reduces and becomes almost negligible if the gap diameter is greater than 250 nm. In this limit we can observe the individual resonance peaks corresponding to individual particles as indicated by the black arrows on top of Fig. 6. Note that these resonance peaks correspond to individual particles, not the sub-array itself, because individual particles of each sub-array are also separated from each other and behave like isolated particles. Furthermore by comparing the individual peaks of S_1, S_2, and S_3 in Fig. 4(a) with the upper row of Fig. 6 as highlighted with the black arrows, we can

infer that the peaks of individual particles also shift to longer wavelengths due to the coupling within the sub-arrays. The results in Fig. 6 show that the coupling between the fundamental modes of the particles is responsible for shaping the AFE spectrum of the combined structure. Note that the fundamental mode of each particle is excited as indicated with the black arrows, but these modes shift due to coupling between the particles.

As discussed above, the spectral shape of the honeycomb structure originates from interaction between fundamental modes of individual particles. These features can also be identified from Fig. 6. As the gap size decreases, interaction between the particles increases. These interactions form two peaks. Strong coupling between S_2 and S_3 or in the particle sense strong coupling between particles with length L_2 and L_3 pushes away the resonance peaks of these particles. As a result, the resonance peak of the particle with length L_2 merges with resonance peak of the particle with length L_1 and forms the first peak at shorter wavelengths and the resonance peak of particle with length L_3 forms the second peak at longer wavelengths. At the same time, as the gap size decreases, the first peak at shorter wavelengths shifts to longer wavelengths. This shift is attributed to coupling between particles within the individual sub-arrays S_1 and S_2. This is also the case for the second peak. But since the coupling between the particles with lengths L_2 and L_3 and the coupling between the particles with length L_3 within sub-array S_3 shift the resonance peak of L_3 in the same direction, it is difficult resolve these two effects.

Due to the strong interaction between S_2 and S_3 the peak of S_3 splits away from the first peak and this leads to a dip in the spectral response. Such a dip may prevent the multiple peaks from forming a distribution that can be defined by a single full-width half-maximum. Therefore, for a flat-top uniform spectral distribution in a broadband application, the dip is an unwanted feature in the region of interest.

4. Generalized close-packed honeycomb array

Based on the results of the previous section, geometrical parameters of the unit cell may provide challenges in obtaining a uniform and broadband field enhancement. To overcome these limitations, we propose a generalized plasmonic honeycomb nanoantenna array through adjustable morphological parameters within the unit cell, which can be incorporated into a large family of plasmonic surfaces. A schematic representation of a generalized plasmonic honeycomb nanoantenna array is shown in Fig. 7 with its associated parameters. In the limiting case as $\beta_1 \to 0^\circ$, $\beta_2 \to 0^\circ$, and $\beta_3 \to 0^\circ$, this structure becomes a honeycomb array containing rod like particles. In the other limiting case as $\beta_1 \to \alpha_1$, $\beta_2 \to \alpha_2$, and $\beta_3 \to \alpha_3$, the structure becomes an aperture array. In this part of the study, the thickness, t, and the width, w, of the gold nanoantennas and the gap diameter, g, are chosen as 20 nm, 10 nm and 30 nm respectively. The length of the particles, i.e. L_1, L_2 and L_3 are also kept constant as 180 nm, 210 nm and 250 nm and the AFE spectrum of the honeycomb antenna array is investigated by varying the apex angles of the particles, i.e. β's. As discussed below, the β parameter is an effective parameter to tune the spectral response without imposing significant restrictions on Wigner–Seitz cell morphology.

Fig. 8 illustrates the effect of changing the β parameters on tailoring the spectrum. In Fig. 8, the β parameters for different particles have been systematically changed to tune the AFE spectrum. In Fig. 8(a), as β_1 was increased the magnitude of the first peak decreased and a new peak at a shorter wavelength appeared as shown by black, red and blue arrows for different β_1's, respectively. Based on the discussions in the previous section, the first peak is formed due to the interaction of the S_1 and S_2 subarrays. Therefore from Fig. 8(a) we can understand that an increase in β_1 shifts the fundamental mode of the particle with length L_1 to shorter wavelengths. Hence the contribution of L_1 in the first peak is removed and leads to a reduction in the magnitude of the first peak of the honeycomb array (green curve of Fig. 8(a)). We also observe this phenomena in Fig. 8(b) and (c). As we increase β_2 (or β_3), the fundamental resonance peak of L_2 (or L_3) shifts to a shorter wavelength as indicated by black, red and blue arrows. In Fig. 8(b), as we increase β_2 a new peak at a shorter wavelength appears as shown by black, red and blue arrows. There is also a change in the second peak of the honeycomb array in Fig. 8(b). This can be attributed to strong coupling between L_2 and L_3. This is due to the fundamental resonance peak of the L_2 change, which in turn effects the peak of L_3 due to the strong coupling. In Fig. 8(c), we changed β_3 and observed that the resonance peak of L_3 shifts to shorter wavelengths. Again, due to the strong coupling between L_2 and L_3,

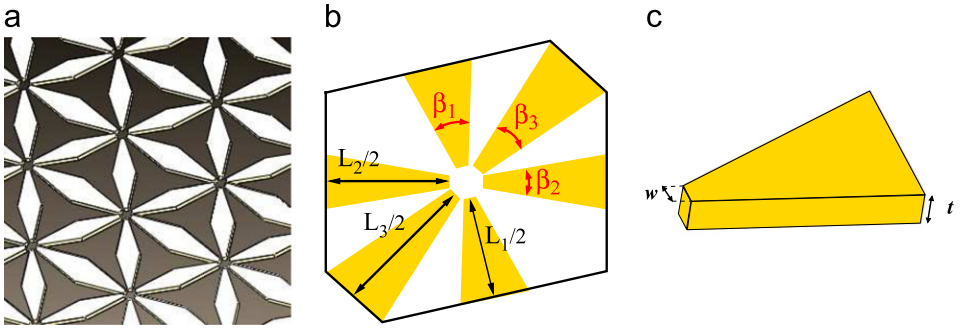

Fig. 7. Generalized close-packed honeycomb array consists of additional parameters (a) corresponding unit cell (b), and an oblique view of an individual particle (c).

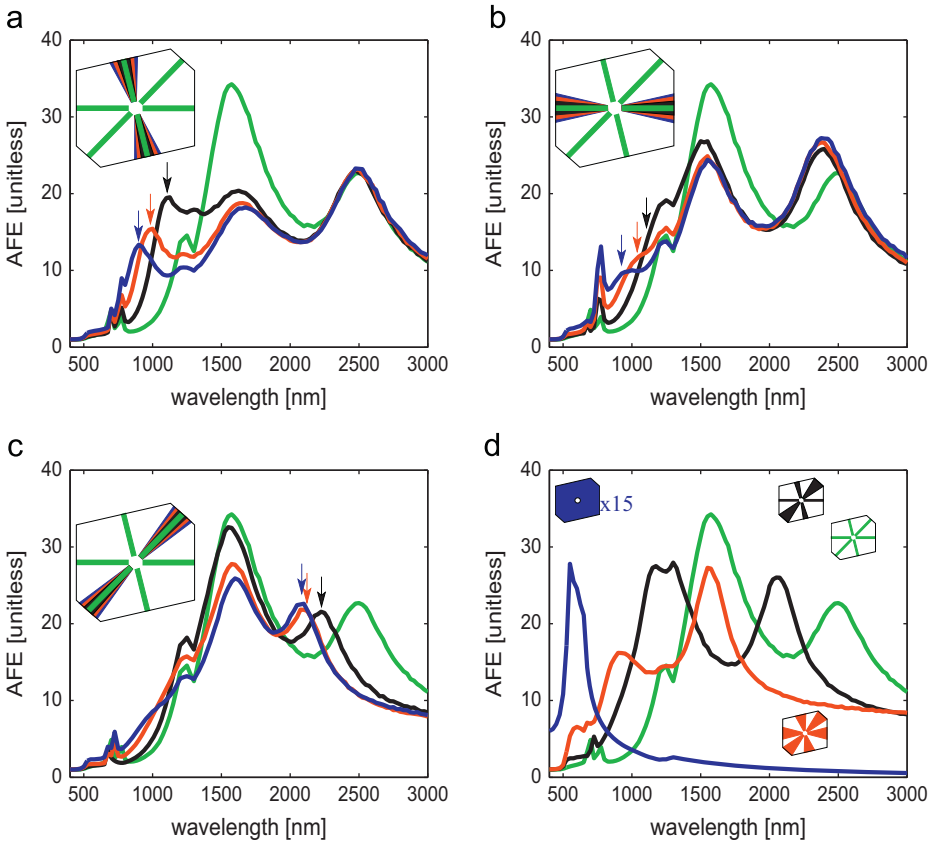

Fig. 8. Tailoring the spectral response with β_1 parameter, corresponding values are 0° (green), 5° (black), 10° (red), 15° (blue) (a), Tailoring the spectral response with β_2 parameter, corresponding values are 0° (green), 5° (black), 10° (red), 15° (blue) (b), Tailoring the spectral response with β_3 parameter, corresponding values are 0° (green), 2.5° (black), 7.5° (red), 12.5° (blue) (c), Tailoring the spectral response with all three β parameters, corresponding values are $(\beta_1\ \beta_2\ \beta_3) = (0^\circ\ 0^\circ\ 0^\circ)$ (green), $(5^\circ\ 0^\circ\ 12.5^\circ)$ (black), $(15^\circ\ 15^\circ\ 12.5^\circ)$ (red) and aperture array (blue) (spectral response of aperture array is multiplied by 15) (d). For all cases the thickness width and lengths of the gold nanoantennas are 20 nm, 10 nm and [180 210 250] nm respectively, and the gap diameter is 30 nm. (For interpretation of the references to color in this figure caption, the reader is referred to the web version of this article.)

increasing β_3 also has an effect on the first peak. Based on these observations in Fig. 8(a)–(c), as the apex angle of a particle is increased, the fundamental resonance peak of that particle shifts to shorter wavelengths since the resonances of the nanoparticles are strongly geometry dependent. The tunability of the overall spectrum through β parameters is very effective as shown in Fig. 8(d). The spectrum can be tailored over a very large range, including spectral broadening and shifting, as shown in Fig. 8(d) with the limiting cases.

The spectral distributions in Fig. 8 indicate that β_3 is a good parameter to adjust in order to remove the unwanted dip. In other words, almost uniform or flat-top spectral distributions can be achieved by properly adjusting β_3. The effect of β_3 on the uniformity of the overall spectra is further investigated in Fig. 9. As β_3 increases, the second peak formed by L_3 approaches to the first peak at shorter wavelengths and shifts the dip well above the full width half maximum, providing a broad and uniform spectral field enhancement.

Another advantage of adjusting the spectral response via β parameters over adjusting it with particle lengths is that significant spectral broadening can be achieved with

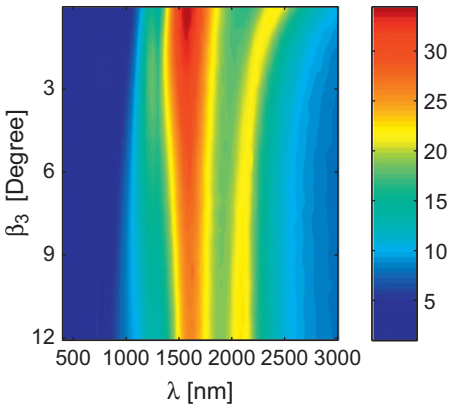

Fig. 9. AFE of a close packed honeycomb array with respect to β_3. The thickness, width, and the lengths of the gold nanoantennas are 20 nm, 10 nm, and [180 210 250] nm respectively.

a symmetric grid. In other words, symmetry breaking of the morphology can be achieved within Wigner–Seitz unit cells whereas the hexagonal grid can be kept symmetric. Fig. 10 illustrates the spectral distributions for

honeycomb antenna arrays where the hexagonal unit cell structure is symmetric but the β parameters are adjusted to create asymmetry within the unit cell. In Fig. 10, the thickness, t, width, w and, the length of the particles, [L_1 L_2 L_3] are chosen as 20 nm, 10 nm and [180 180 180] nm respectively and the gap diameter, g, is 30 nm. Beta parameters are chosen as (0°, 0°, 0°), (1°, 2°, 3°), (0°, 3°, 6°) and (0°, 5°, 10°) for the green, black, red and blue curves respectively in Fig. 10. As shown in Fig. 10, a broader spectrum over the symmetric hexagonal lattice is achieved by varying the β parameters while keeping the particle length constant.

5. Advantages of close-packed arrays

Honeycomb plasmonic antenna arrays in Figs. 1 and 7 are close-packed structures such that each particle is shared between the adjacent unit cells. In other words, each particle is a member of two adjacent unit cells. Such a close-packed antenna array has advantages. A close-packed arrangement of an antenna array maximizes the number of particles per unit area, and therefore, increases the field enhancement per unit area. In addition, a close-packed structure has stronger coupling between neighboring unit cells, which supports the broadening of the spectral distributions. These advantages of close-packed arrays are illustrated in Fig. 11, where the spectral distributions of an array of nanoantennas are compared for different packing ratios. In Fig. 11(a), the unnormalized spectrum of a high-packing fraction antenna array is compared with that of a low-packing ratio antenna array. In Fig. 11(a), the thickness, t, width, w and length of the antennas, [L_1 L_2 L_3] are 20 nm, 10 nm and [100 100 100] nm respectively and the gap diameter, g, is 30 nm. The unnormalized spectrum in Fig. 11(a) indicates that the enhancement of the close-packed array is 7.8 times larger. Another important consequence of close packing is as the distance between the particles decreases, due to radiation damping, full width at half maximum (FWHM) increases leading to a broader spectral response [39,40]. In Fig. 11(b), the spectra of high and low packing fraction arrays are compared on the same scale in order to compare their line widths. The FWHM of the close-packed array is 270 nm whereas the FWHM of the non-close packed array is only 94 nm. This result shows that as maximum field enhancement is obtained via close packing at the same time it also provides a broader spectral response.

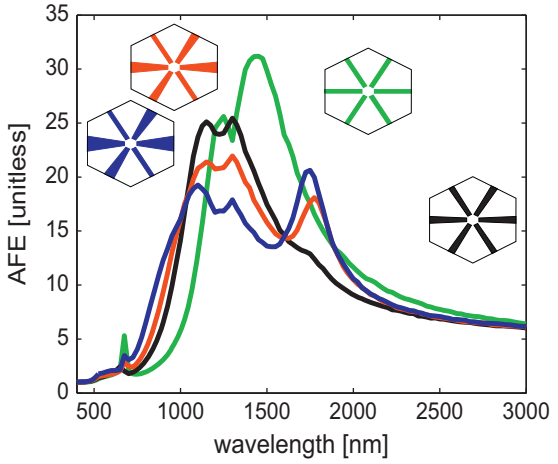

Fig. 10. Broadening the spectral response of a symmetric honeycomb array via β parameters. The thickness, width, and the length of the gold nanoantennas are 20 nm, 10 nm, and [180 180 180] nm, respectively; and the gap diameter is 30 nm. Beta parameters are chosen as (0°, 0°, 0°), (1°, 2°, 3°), (0°, 3°, 6°), and (0°, 5°, 10°) for the green, black, red, and blue curves respectively. (For interpretation of the references to color in this figure caption, the reader is referred to the web version of this article.)

6. Radiative properties of honeycomb arrays

In this section, we discuss the radiative properties of honeycomb plasmonic nanoantenna arrays, such as absorptance, transmittance, and reflectance. In Fig. 12, absorptance, transmittance, and reflectance of a honeycomb are shown with red, black, and blue curves, respectively. The results are obtained for an optical beam that excites the nanoantenna array at normal incidence. As shown in Fig. 12, the calculations are performed for

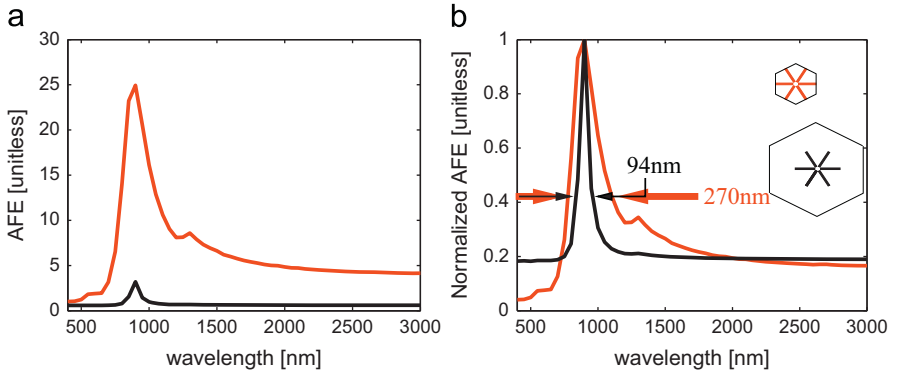

Fig. 11. Comparison of spectral responses of a close-packed and nonclose-packed arrangement of honeycomb arrays. (a) Field enhancement and (b) spectral broadening is observed for the close-packed arrangement. In both cases symmetrical honeycomb arrays are used and the thickness, width, and length of the gold nanoantennas are 20 nm, 10 nm, and [100 100 100] nm respectively and the gap diameter is 30 nm. In the nonclose packed case the distance between the snowflake centers is 1300 nm which is 10 times greater than the close packed case.

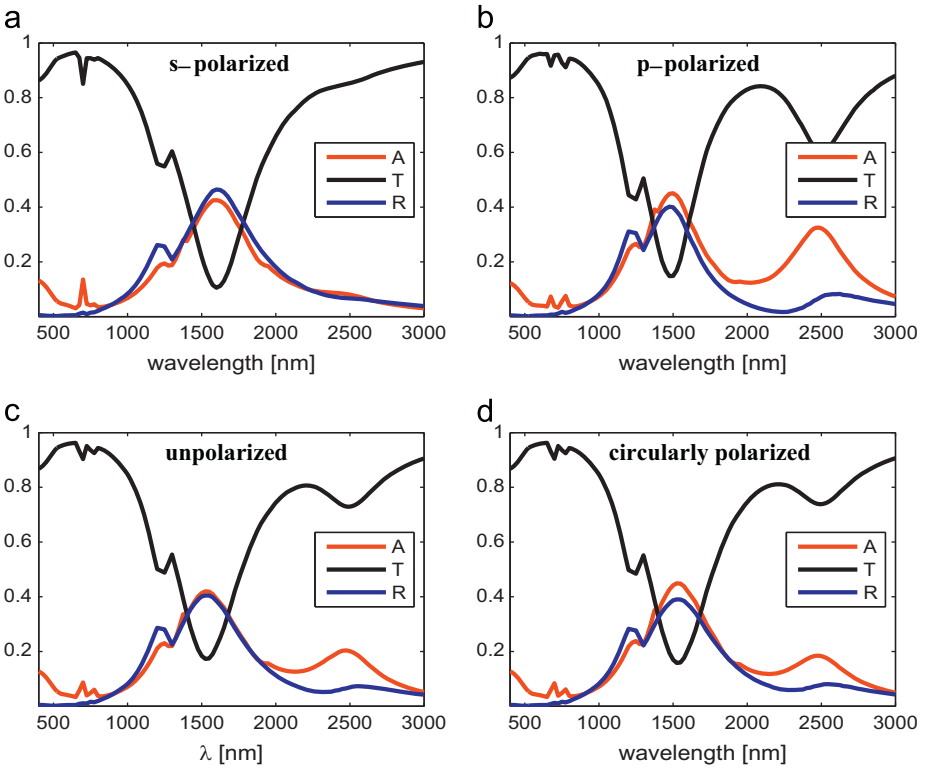

Fig. 12. Far-field radiative properties of honeycomb arrays. Red, black, and blue curves represent absorptance, transmittance, and reflectance, respectively for different polarization states. (For interpretation of the references to color in this figure caption, the reader is referred to the web version of this article.)

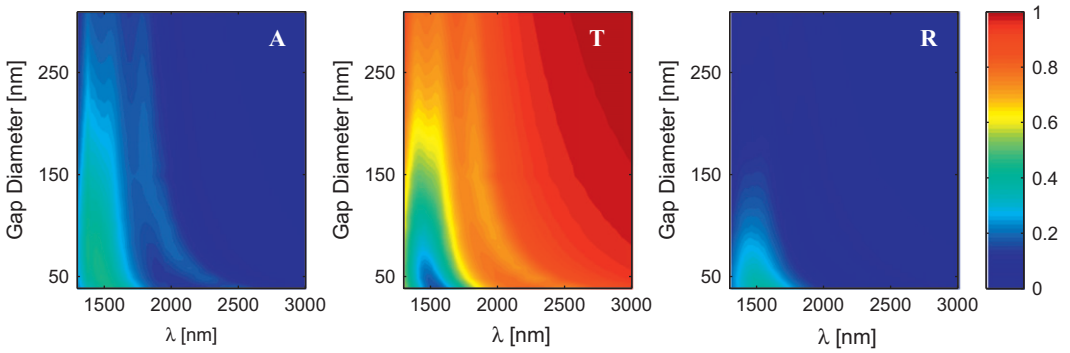

Fig. 13. Far-field radiative properties of honeycomb arrays as a function of wavelength and gap diameter. Absorption (A), reflection (R), and transmission (T) are plotted for unpolarized beam.

s-polarized, p-polarized, unpolarized, and circularly polarized beams. To calculate the radiative properties of the honeycomb array, the geometrical dimensions of the structure in Fig. 12 are selected as identical to that of Fig. 4. In Fig. 12(a), the incident field is s-polarized. In this case, the incident field polarization is parallel to the long axis of the particle with length L_2, but the incident field polarization also has a weak component that is parallel to the long axes of other particles. As a result the first peak formed by particles with lengths L_1 and L_2 is observable but the second peak formed by particle with length L_3 is weak. The far-field properties for the p-polarized incident field are illustrated in Fig. 12(b). In this case incident polarization has components parallel to the long axes of particles with lengths L_1 and L_3 but has no component parallel to the long axis of the particle with length L_2. As a result both resonance peaks are observable. Since the particle with length L_2 is not exited, the first peak is narrow compared to the spectrum given in Fig. 12(a). In Fig. 12(c) and (d), the far-field responses of the honeycomb array are illustrated when it is illuminated with unpolarized and circularly polarized fields,

respectively. In these cases all of the particles can be excited effectively and as a result both peaks can be observed.

In Fig. 12, there are differences between absorptance and reflectance spectra, which can be attributed to absorption and scattering cross-sections of particles [41,42]. This difference is especially significant in Fig. 12(b)–(d) for longer wavelengths where the effect of particle with length L_3 is dominant. As the particle gets longer it absorbs more light than it scatters. Therefore there is an increase in absorptance at longer wavelengths. On the other hand, around the first peak the difference is not so prominent because the absorption and scattering cross-sections of particles with lengths L_1 and L_2 are close to each other. The mechanisms that form the spectral features of radiative properties in Fig. 12 are similar to those discussed for the AFE spectrum. In Fig. 13, the radiative properties of the honeycomb structure as a function of both the gap diameter and wavelength are given in Fig. 13. The interaction between antenna elements L_1, L_2, and L_3 with each other and across the gap play a significant role for radiative properties as well, similar to the coupling discussion in Section 3.

7. Conclusion

In this study, we proposed a generalized close-packed honeycomb array by introducing additional morphological parameters within the Wigner–Seitz unit cell. The generalized honeycomb plasmonic antenna array provides additional flexibility in the manipulation of the spectral response via these new morphological parameters by relaxing geometrical restrictions due to particle length and angles within the Wigner–Seitz unit cell. By using the proposed structures, we demonstrated that the wideband spectral distribution can be effectively tailored over large scale surfaces. An alternative technique for breaking the symmetry of plasmonic honeycomb antenna arrays was suggested. It was demonstrated that spectral broadening can also be achieved by breaking the symmetry within the Wigner–Seitz unit cell on a hexagonal grid, rather than breaking the symmetry of the hexagonal grid itself. Another important aspect of this study is the demonstration of advantages of close-packing of the antenna arrays in terms of spectral response, field enhancement, and absorption over a large surface area. Coupling-mechanisms shaping the spectral lines of the large scale surfaces were shown by decomposing the overall spectrum into contributions from sub-arrays.

References

[1] Alivisatos AP. Semiconductor clusters, nanocrystals, and quantum dots. Science 1996;271(5251):933–7.
[2] Huynh WU, Dittmer JJ, Alivisatos AP. Hybrid nanorod-polymer solar cells. Science 2002;295(5564):2425–7.
[3] Yablonovitch E, Gmitter TJ, Leung KM. Photonic band structure: the face-centered-cubic case employing nonspherical atoms. Phys Rev Lett 1991;67:2295–8.
[4] Halas NJ. Plasmonics: an emerging field fostered by nano letters. Nano Lett 2010;10(10):3816–22.
[5] Prodan E, Radloff C, Halas NJ, Nordlander P. A hybridization model for the plasmon response of complex nanostructures. Science 2003;302(5644):419–22.
[6] Nordlander P, Oubre C, Prodan E, Li K, Stockman MI. Plasmon hybridization in nanoparticle dimers. Nano Lett 2004;4(5):899–903.
[7] Fan JA, Wu C, Bao K, Bao J, Bardhan R, Halas NJ, et al. Self-assembled plasmonic nanoparticle clusters. Science 2010;328(59):1135–8.
[8] Ebbesen T, Lezec HJ, Ghaemi HF, Thio T, Wolff PA. Extraordinary optical transmission through sub-wavelength hole arrays. Nature 1998;391:667–9.
[9] Schuller JA, Barnard ES, Cai W, Jun YC, White JS, Brongersma ML. Plasmonics for extreme light concentration and manipulation. Nat Mater 2010;9:193–204.
[10] Papasimakis N, Fedotov VA, Zheludev NI, Prosvirnin SL. Metamaterial analog of electromagnetically induced transparency. Phys Rev Lett 2008;101:253903.
[11] Liu N, Langguth L, Weiss T, Kastel J, Fleischhauer M, Pfau T, et al. Nat Mater 2009;8:758–62.
[12] Shalaev VM, Cai W, Chettiar UK, Yuan HK, Sarychev AK, Drachev VP, et al. Negative index of refraction in optical metamaterials. Opt Lett 2005;30(24):3356–8.
[13] Barnes WL, Dereux A, Ebbesen TW. Nature 2003;424:824–30.
[14] Ozbay E. Plasmonics: merging photonics and electronics at nanoscale dimensions. Science 2006;311(5758):189–93.
[15] Stockman MI. Nanoplasmonics: past, present, and glimpse into future. Opt Express 2011;19(22):22029–106.
[16] Novotny L, van Hulst N. Antennas for light. Nat Photonics 2011;5:83–90.
[17] Giannini V, Fernandez-Dominguez AI, Heck SC, Maier SA. Plasmonic nanoantennas: fundamentals and their use in controlling the radiative properties of nanoemitters. Chem Rev 2011;111(6):3888–912.
[18] Yu N, Genevet P, Kats MA, Aieta F, Tetienne JP, Capasso F, et al. Light propagation with phase discontinuities: generalized laws of reflection and refraction. Science 2011;334(6054):333–7.
[19] Francoeur M, Menguc MP, Vaillon R. Near-field radiative heat transfer enhancement via surface phonon-polaritons coupling in thin films. Appl Phys Lett 2008;93:043109.
[20] Rousseau E, Siria A, Jourdan G, Volz S, Comin F, Chevrier J, et al. Radiative heat transfer at the nanoscale. Nat Photonics 2009;3:514–7.
[21] Shen S, Narayanaswamy A, Chen G. Surface phonon polaritons mediated energy transfer between nanoscale gaps. Nano Lett 2009;9:2909–13.
[22] Sendur K, Baran E. Near-field power transmission of dipole nano-antennas. Appl Phys B 2009;96:325–35.
[23] Sendur K, Kosar A, Menguc MP. Localized radiative energy transfer from a plasmonic bow-tie nano-antenna to a magnetic thin film stack. Appl Phys A 2011;103:703–7.
[24] Atwater H, Polman A. Plasmonics for improved photovoltaic devices. Nat Mater 2010;9:205–13.
[25] Nevet A, Berkovitch N, Hayat A, Ginzburg P, Ginzach S, Sorias O, et al. Plasmonic nanoantennas for broad-band enhancement of two-photon emission from semiconductors. Nano Lett 2010;10(5):1848–52.
[26] Shegai T, Miljkovi VD, Bao K, Xu H, Nordlander P, Johansson P, et al. Unidirectional broadband light emission from supported plasmonic nanowires. Nano Lett 2011;11:706–11.
[27] Volpe G, Quidant R. Fractal plasmonics: subdiffraction focusing and broadband spectral response by a sierpinski nanocarpet. Opt Express 2011;19(4):3612–8.
[28] Unlu ES, Tok RU, Sendur K. Broadband plasmonic nanoantenna with an adjustable spectral response. Opt Express 2011;19:1000–6.
[29] Tok RU, Ow-Yang C, Sendur K. Unidirectional broadband radiation of honeycomb plasmonic antenna array with broken symmetry. Opt Express 2011;19(23):22731–42.
[30] Aubry A, Lei DY, Fernandez-Domainguez AI, Sonnefraud Y, Maier SA, Pendry JB. Plasmonic light-harvesting devices over the whole visible spectrum. Nano Lett 2010;10(7):2574–9.
[31] Ni X, Emani NK, Kildishev AV, Boltasseva A, Shalaev VM. Broadband light bending with plasmonic nanoantennas. Science 2012;335(6067):427.
[32] Pala RA, White J, Barnard E, Liu J, Brongersma ML. Design of plasmonic thin-film solar cells with broadband absorption enhancements. Adv Mater 2009;21(34):3504–9.

[33] Aydin K, Ferry V, Briggs R, Atwater H. Broadband polarization-independent resonant light absorption using ultrathin plasmonic super absorbers. Nat Commun 2011;2:517.
[34] Sendur K, Peng C, Challener W. Near-field radiation from a ridge waveguide transducer in the vicinity of a solid immersion lens. Phys Rev Lett 2005;94:043901.
[35] Sendur K, Challener W, Peng C. Ridge waveguide as a near-field aperture for high density data storage. J Appl Phys 2004;96:2743–52.
[36] Palik ED. Handbook of optical constants of solids. New York, NY: Academic Press; 1998.
[37] Balanis CA. Advanced engineering electromagnetics. New York, NY: Wiley; 1989. pp. 1–41.
[38] Rahmani M, Lei DY, Giannini V, Lukiyanchuk B, Ranjbar M, Liew TYF, et al. Subgroup decomposition of plasmonic resonances in hybrid oligomers: modeling the resonance lineshape. Nano Lett 2012;12(4):2101–6.
[39] Mikhailov S. Radiative damping of collective excitations in periodic arrays of quantum wires and dots. Superlattice Microst 1998;23(2):345–8.
[40] Dahmen C, Schmidt B, von Plessen G. Radiation damping in metal nanoparticle pairs. Nano Lett 2007;7(2):318–22.
[41] Qiu L, Larson TA, Smith DK, Vitkin E, Zhang S, Modell MD, et al. Single gold nanorod detection using confocal light absorption and scattering spectroscopy. IEEE J Sel Top Quant 2007;13(6):1730–8.
[42] Qiu L, Larson TA, Vitkin E, Guo L, Hanlon EB, Itzkan I, et al. Single gold nanorod detection using confocal light absorption and scattering spectroscopy. Opt Lett 2010;1(1):135–42.